# PKR activation-induced mitochondrial dysfunction in HIV-transgenic mice with nephropathy

Teruhiko Yoshida[1*#], Khun Zaw Latt[1#], Avi Z. Rosenberg[2], Briana A. Santo[3], Komuraiah Myakala[4], Yu Ishimoto[5], Yongmei Zhao[6], Shashi Shrivastav[1], Bryce A. Jones[4], Xiaoping Yang[2], Xiaoxin X. Wang[4], Vincent M. Tutino[3], Pinaki Sarder[3,7], Moshe Levi[4], Koji Okamoto[1,8], Cheryl A. Winkler[6], Jeffrey B. Kopp[1]

[1] Kidney Disease Section, Kidney Diseases Branch, NIDDK, NIH, Bethesda, MD [2]Department of Pathology, Johns Hopkins Medical Institutions, Baltimore, MD [3]Department of Pathology and Anatomical Sciences, Jacobs School of Medicine & Biomedical Sciences, University at Buffalo, Buffalo, NY [4]Department of Biochemistry and Molecular & Cellular Biology, Georgetown University, Washington, DC [5]Polycystic Kidney Disease Section, Kidney Diseases Branch, NIDDK, NIH, Bethesda, MD [6]Frederick National Laboratory for Cancer Research, NCI, NIH, Frederick, MD [7]College of Medicine, University of Florida, Gainesville, FL [8]Nephrology Endocrinology and Vascular Medicine, Tohoku University Hospital, Sendai, Japan

[#] These authors contributed equally to this manuscript.

*Corresponding author:* Teruhiko Yoshida, MD PhD; *address:* 10 Center Dr. 3N104, Bethesda, MD 20892-1268; *phone:* 301-496-2988; *email:* teruhiko.yoshida@nih.gov.

Running Title: PKR activation in HIV-associated nephropathy mice

## Abstract

HIV remains prevalent in the USA and chronic kidney disease remains a major cause of morbidity in HIV-1-positive patients. Host double-stranded RNA (dsRNA)-activated protein kinase (PKR) is a sensor for viral dsRNA, including HIV-1. We show that PKR inhibition by compound C16 ameliorates the HIV-associated nephropathy (HIVAN) kidney phenotype in the Tg26 transgenic mouse model, with reversal of mitochondrial dysfunction. Combined analysis of single-nucleus RNA-seq and bulk RNA-seq data revealed that oxidative phosphorylation was one of the most downregulated pathways and identified Stat3 as a potential mediating factor. We identified in Tg26 mice a novel proximal tubular cell cluster enriched in mitochondrial transcripts. Podocytes showed high HIV-1 gene expression and dysregulation of cytoskeleton-related genes and these cells dedifferentiated and were lost. Cell-cell interaction analysis suggested that the profibrogenic PKR-STAT3-PDGF-D pathway was activated in injured proximal tubules and was triggered by PDGFRB-expressing fibroblasts throughout the cortex. These findings suggest that PKR inhibition and mitochondrial rescue as potential novel therapeutic approaches for HIVAN.

**Keywords**; HIV, PKR, HIV-associated nephropathy, mitochondria, single-nucleus RNA-seq, RNA-seq

## Translational Statement

This work highlighted mitochondrial dysfunction in HIV-associated nephropathy mice kidney by combination of single-nuclear and bulk RNA-seq analysis. We ameliorated the kidney damage by PKR inhibitor C16 treatment showing mitochondrial rescue by transcriptomic profiling and functional assay. This transcriptomic-driven characterization showed that PKR inhibition and mitochondrial rescue as potential therapeutic approaches for HIV-associated nephropathy.

## Introduction

In 2020, approximately 37 million people were living with HIV, an estimated 680,000 people globally died from HIV-related causes, and approximately 1.5 million people became newly infected with HIV, according to the World Health Organization (WHO).[1] HIV remains prevalent in the US[2] and even more highly prevalent in sub-Saharan Africa, especially in East and Southern Africa.[3] Chronic kidney disease remains one of the major causes of morbidity in HIV-1 positive patients, even with the widespread availability of combined anti-retroviral therapy.[4] The most severe form of kidney disease in persons with untreated or undertreated HIV infection is HIV-nephropathy (HIVAN), a form of collapsing glomerulopathy. Therapy for HIVAN includes combined anti-retroviral therapy, coupled with RAAS blockade to prevent chronic kidney disease progression. There is as yet not specific therapy for HIVAN.[5,6]

The Tg26 transgenic mouse model has been well-studied and established as the standard mouse model of HIV-associated nephropathy (HIVAN). HIV-1 transgene expression in kidney cells induces the HIVAN phenotype.[7] The mice manifest similar histological features of human HIVAN, including collapsing glomerulopathy, microtubular dilatation and interstitial fibrosis. Mice with HIVAN develop progressive renal dysfunction with evolution to terminal uremia, if the mice are not euthanized.[8,9]

Many therapeutic approaches have been shown to be effective for kidney diseases in the Tg26 model. These include inhibitors of mammalian target of rapamycin (mTOR),[10-12] a Notch inhibitor,[13,14] renin angiotensin system inhibition,[15,16] cyclin-dependent kinase inhibitor,[17] SIRT1 agonist or overexpression,[18] STAT3 activation reduction,[19,20] retinoic acid receptor agonist,[21] and

NF-kB inhibition.[22] Recent reports have identified several injury pathways, including NLRP3[23] and mitochondrial dysfunction.[24,25] Further, bulk multi-omics approach using mRNA microarrays and protein-DNA arrays[26] identified HIPK2 as a the regulator of Tg26 renal pathology; this was confirmed by additional recent reports.[27,28] A mRNA microarray approach characterized bulk transcriptional profiles during progressive renal disease.[29] While these reports have provided novel insights into tissue transcriptional dynamics, to date no studies have been performed at single-cell or single-nucleus resolution.

Double-stranded RNA (dsRNA)-activated protein kinase (PKR) is a sensor for dsRNA and is activated in response to viral infections, including HIV-1. In the US, HIV remains an important problem that disproportionately affects marginalized groups, including the Black/African-American community.[1] *APOL1* risk variants, exclusively present in individuals with recent sub-Saharan ancestry, damage podocytes through various mechanisms including double-stranded RNA-activated protein kinase (PKR) activation by *APOL1* mRNA.[30] PKR inhibition using the oxoindole/imidazole compound C16 has been reported to be beneficial in neuroinflammatory disease models.[31,32]

Here, we hypothesize that PKR activation could be a mechanistic pathway shared by HIV- and APOL1-mediated nephropathies, considering the high odds ratio for HIVAN among African Americans (OR 29) and South Africans (OR 89) carrying two *APOL1* risk alleles.[33] Hence, we investigated the effects of PKR inhibition in the Tg26 HIVAN mouse model, which expresses HIV regulatory and accessory genes. We used single-nucleus and bulk RNA-sequencing

methods to describe transcriptional changes between treatment groups and to uncover associated molecular mechanisms in an unbiased fashion.

## Methods

*Mice*

We studied both male and female mice, aged 6–12 weeks. Mice in treatment groups were matched for sex. Hemizygous ($Tg26^{+/-}$) male mice were bred with wild type FVB/N female mice to generate Tg26 hemizygote mice for experiments. Transgenic mice were identified by PCR genotyping.

For PKR inhibition treatment with C16, the C16 treatment group mice received 10 µg/kg body weight of C16 (Sigma, Darmstadt, Germany) in 10 ml/kg body weight 0.5% DMSO-PBS intraperitoneally three times a week from 6 weeks to 12 weeks of age. Urine collection (by 24-hour metabolic cage collection) and body weight measurement were done at 6 weeks of age before treatment and 12 weeks of age after treatment. All mice were euthanized and kidneys, plasma, serum samples were collected at age of 12 weeks for further characterization as described.

*Mouse chemistry measurements*

Plasma creatinine was measured by isotope dilution LC-MS/MS at The University of Alabama at Birmingam O'Brien Center Core C (Birmingham, AL). Urine albumin levels were measured using Albuwell M ELISA kits (Ethos Biosciences, Newtown Square, PA). Urine creatinine concentrations were measured using the Creatinine Companion kit (Ethos Biosciences, Newtown Square, PA). Urinary NGAL and KIM-1 were measured by the Mouse Lipocalin-2/NGAL DuoSet ELISA and Mouse TIM-1/KIM-1/HAVCR Quantikine ELISA Kit (R&D Systems, Minneapolis, MN). All measurements were conducted with technical duplicates. Urinary

measurements were expressed as the ratio of the concentrations of analytes to the urine creatinine concentrations. Investigators were masked when assessing outcomes.

*Mouse kidney pathological evaluation*

Formalin-fixed, paraffin-embedded mouse kidney tissue sections, cut at 4 μm, were stained with hematoxylin and eosin, periodic acid Schiff, and Picrosirius Red.

*In situ hybridization of mouse kidneys*

Chromogenic *in situ* detection of RNA was performed using RNAscope (Advanced Cell Diagnostics, Biotechne, Minneapolis, MN). Briefly, 5 μm tissue sections were de-paraffinized, boiled with RNAscope target retrieval reagent for 15 min and protease digested at 40 °C for 30 min, followed by hybridization for 2 h at 40 °C with RNA probe Mm-mt-Co1, Mm-mt-Atp6 (catalog # 517121, 544401). RNA probe-Mm-PPIB (catalog # 313911) and RNA Probe-DapB (catalog # 310043) were used for positive and negative control, respectively. Specific probe binding sites were visualized using RNAscope 2.5 HD Reagent Kit (catalog # 322310).

*Immunohistochemistry in mouse kidneys*

Mouse kidney tissues were fixed with 10% buffered formalin for 24 hours, embedded in paraffin, and sectioned at 4-5 μm. The sections were deparaffinized/rehydrated and antigen retrieval was performed by heating in citrate-buffered medium for 15 min in a hot water bath. Tissues were blocked with 2.5% normal horse serum for 20 mins. Sections were incubated for 1 h at room temperature with primary antibody against phospho-Stat3 (Tyr705) (#9145, 1:100 dilution, Cell

Signaling, Danvers, MA), and platelet-derived growth factor (PDGF)-D (ab181845, Abcam, 1:100 dilution, Cambridge, UK). Sections were processed following ImmPRESS HRP Universal Antibody (horse anti-mouse/rabbit IgG) Polymer Detection Kit and ImmPACT DAB EqV Peroxidase (HRP) Substrate (Vector Laboratories, Burlingame, CA) protocol, and counter stained with hematoxylin.

*Immunoblotting*

Tissues were lysed in a radioimmunopreciptation assay (RIPA) buffer (Thermo Fisher Scientific, Waltham, MA) containing a protease inhibitor/ phosphatase inhibitor cocktail (#78440, Thermo Fisher Scientific, Waltham, MA). Lysates were separated by SDS-polyacrylamide gel electrophoresis (SDS-PAGE) (gradient gel 4-12%, MOPS buffer) and the proteins subjected to Western blotting and blocked for one hour in Odyssey blocking buffer (LI-COR, Lincoln, NE). Blots were incubated following the protocol of iBind (Thermo Fisher Scientific, Waltham, MA). Primary antibodies were Phospho-Stat3 (Tyr705) (#9145, 1:2000 dilution, Cell Signaling, Danvers, MA), Stat3 (#9139, 1:1000 dilution, Cell Signaling, Danvers, MA), β-actin (#47778, 1:5000 dilution, Santa Cruz Biotechnology, Dallas, TX), Total OXPHOS Rodent (#ab110413, 1:250 dilution, Abcam, Cambridge, UK), VDAC (# 4661, 1:1000 dilution, Cell Signaling, Danvers, MA). All blots were imaged using the Odyssey infrared scanner (LI-COR, Lincoln, NE). SDS-PAGE gel images are shown in Supplemental figures.

*Glomerular and proximal tubule enrichment method*

Mice were anesthetized using 2, 2, 2-trimbromoethanol (Avertin) and the abdominal aorta and vena cava were exposed. After clipping the abdominal aorta distal to renal artery bifurcation, a

catheter was inserted into the aorta proximal to an incision above iliac artery bifurcation. After clipping the celiac trunk, superior mesenteric artery, and thoracic aorta proximal to renal arteries bifurcation, a small incision was made in the renal vein to perfuse both kidneys with 1 ml of PBS. Next, kidneys were perfused twice with 10 ul of Dynabeads M-450 Tosylactivated (#14013, Thermo Fisher Scientific, Waltham, MA), to facilitate isolation of glomeruli.

Kidneys were immediately collected, decapsulated, and placed into Hanks Balanced Salt Solution (HBSS) medium on ice. Kidneys were minced using razor blades and enzymatically digested in 1 mL of HBSS containing 4 mg collagenase A (#10103586001, Sigma, Darmstadt, Germany) and 40 μl DNase I recombinant (E04716728001, Sigma, Darmstadt, Germany) for 30 mins at 37 °C with shaking at 1500 rpm.

Glomerular samples were collected after filtration through a 100 μm strainer, followed by magnetic separation (MPC-S, DYNAL) and three PBS washes. Proximal tubular samples were collected from the non-glomerular supernatant of the first magnetic separation step. Proximal tubules were isolated by centrifugation through 31% Percoll (17089102, Cytiva, Marlborough, MA)-PBS centrifugation, followed by an additional wash and centrifugation with PBS, following a published protocol.[34,35]

*Bulk RNA-sequencing*

Mouse kidney outer cortex tissues were dissected and homogenized in QIAzol. Total RNA samples were extracted using RNeasy Plus Universal Kit (QIAGEN, Hilden, Germany) following the manufacturer's protocol including removal of genomic DNA step. RNA samples were prepared for library to be sequenced at the Sequencing Facility at Frederick National Laboratory for Cancer Research, NCI.

Samples were pooled and sequenced on NovaSeq6000 S1 flowcell using Illumina TruSeq Stranded mRNA Library Prep and paired-end sequencing with read length 101bps (2x101 cycles). The samples had 46 to 72 million pass filter reads and more than 92% of bases calls were above a quality score of Q30. Reads of the samples were trimmed for adapters and low-quality bases using Cutadapt[36]. The trimmed reads were mapped to reference genome (Mouse - mm10) and transcripts (Ensembl v96 annotation) using STAR aligner. The gene expression quantification analysis was performed for all samples using STAR/RSEM tools. DESeq2 was used for differential expression analysis from raw count data and normalized data were used for Gene set enrichment analysis by GSEA. GSEA v4.1.0 was used for pathway enrichment analysis. Pathway analysis including canonical pathway analysis and upstream regulator analysis were generated through the use of QIAGEN Ingenuity Pathway Analysis.[37]

*Single-nucleus RNA-sequencing*

Nuclei from frozen mouse kidney outer cortex tissue samples and glomeruli-enriched samples were prepared using the following protocol at 4°C[38]: briefly, ~ 8 $mm^3$ tissue fragments were cut by razor blade in EZlysis buffer (#NUC101-1KT, Sigma, Darmstadt, Germany) and homogenized 30 times using a loose Dounce homogenizer and 5 times by tight pestle. After 5 min of incubation, the homogenate was passed through a 40 µm filter (PluriSelect, El Cajon, CA) and centrifuged at 500g at 4°C for 5 min. The pellet was washed with EZlysis buffer (Sigma Aldrich, St Louis, MO) and again centrifuged at 500g at 4°C for 5 min. The pellet was resuspended with DPBS with 1% FBS and passed through a 5 µm filter (PluriSelect, El Cajon, CA) to make final nuclei prep for loading on to a 10xChromium Chip G (10X Genetics, San Francisco, CA) for formation of gel beads in emulsion (GEM).

Single nuclear isolation, RNA capture, cDNA preparation, and library preparation were accomplished following the manufacturer's protocol (Chromium Next GEM Single Cell 3' Reagent Kit, v3.1 chemistry, 10x Genomics, Pleasanton, CA). Prepared cDNA libraries were sent to the Sequencing Facility at Frederick National Laboratory for Cancer Research, NCI, for sequencing. All samples had sequencing yields of more than 245 million reads per sample with over 96.0% of bases in the barcode regions had Q30 or above and at least 89.7% of bases in the RNA read had Q30 or above. More than 95.5% of bases in the UMI had Q30 or above. Analysis was performed with the Cell Ranger v5.0.0 software using the default parameters with pre-mRNA analysis turned on. The reference was built from mm10 reference genome complemented with HIV-1 viral sequences.

*Single-nucleus RNA-seq Analysis*

Integration of single-nucleus gene expression data was performed using Seurat (version 4.0.3) after filtering nuclei with the number of detected genes < 200 or > 4000, the number of total RNA count > 15000 and the percentage of mitochondrial transcripts > 20%. After filtering, 30557 cells remained for downstream analysis. Clustering of the combined data used the first 30 principal components at a resolution of 0.6 and identified 23 distinct cell clusters. Cell type identification was done based on the expression levels of known marker genes. Pseudotime analysis of podocytes and proximal tubule cells was performed by using the R package monocle 3 (version 1.0), considering wild type cells as the root state. Cell-cell interaction analysis was done by using CellphoneDB after converting mouse genes to human orthologs. Cell cycle analysis was performed by converting cell cycle marker genes from Tirosh et al. to mouse orthologs. Pathway analysis including canonical pathway analysis and upstream regulator analysis were generated through the use of QIAGEN Ingenuity Pathway Analysis.[37]

*Seahorse Extracellular Flux Assay*

Seahorse 96-well assay plates (Agilent, Santa Clara, CA) were pre-coated twice with 20 μl/well of 0.01% Poly-L-lysine solution (P4707, Sigma, Darmstadt, Germany) and washed twice with PBS, 200 μl/well. Glomerular or proximal tubular samples were plated with EGM-2 medium (CC-3162, Lonza, Walkersville, MD) and placed in $CO_2$-incubator for 30 mins for the attachment.

Seahorse Mito Stress Tests were conducted as described.[30] Cells were incubated in an $CO_2$-free incubator for 30 min after replacement of medium. Seahorse XF RPMI medium, pH 7.4 (103576-100, Agilent, Santa Clara, CA), was used for glomerular samples and Seahorse XF

DMEM medium, pH 7.4 (103575-100, Agilent, Santa Clara, CA), was used for proximal tubular samples. Medium was supplemented to reach a final concentration of 10 mM glucose, 1mM sodium pyruvate, and 2 mM L-glutamine. Reagent concentrations used were 2 μM oligomycin, 2 μM FCCP, 0.5 μM rotenone and 0.5 μM antimycin A (103015-100, Agilent, Santa Clara, CA).

Data were normalized by total nucleic acid content measured by CyQUANT Cell Proliferation (C7026, Thermo Fisher Scientific, Waltham, MA) and analyzed by Wave 2.6.1 (Agilent, Santa Clara, CA).

*Estimation of glomerular podocyte count*

PodoCount[39], a computational tool for whole slide podocyte estimation from digitized histologic sections, was used to detect, enumerate, and characterize podocyte nuclear profiles in the glomeruli of immunohistochemically labeled (IHC-labeled) murine kidney sections. Formalin-fixed, paraffin embedded tissues (2 μm thickness) were IHC-labeled for $p57^{kip2}$, a marker of podocyte terminal differentiation (ab75974, Abcam, Cambridge, UK), and detected with horse radish peroxidase (RU-HRP1000, Diagnostic BioSystems, Pleasanton, CA) and diaminobenzidine chromogen substrate (BSB0018A, Bio SB, Santa Barbara, CA). A periodic acid-Schiff post-stain was applied without hematoxylin counterstain. The tool uses a combination of stain deconvolution, digital image processing, and feature engineering to compute histologic podometrics [40] with correction for section thickness [41]. In this study, PodoCount was used to assess mean glomerular podocyte count per mouse.

*Statistics*

We conducted t-test for two-group comparisons and one-way ANOVA for comparisons involving more than two groups, with multiple test correction. A P value less than 0.05 was considered significant.

*Study Approval*

All mouse experiments were conducted in accordance with the National Institutes of Health Guide for the Care and Use of Laboratory Animals and were approved in advance by the NIDDK Animal Care and Use Committee (Animal study proposal, K097-KDB-17 & K096-KDB-20).

## Results

*PKR inhibition ameliorates kidney injury in Tg26 mouse*

The TAR (trans-activating region) RNA in HIV-1 long terminal repeats (LTRs) at the 5' and 3' ends are known to form double stranded RNA (dsRNA) structures and activates PKR by inducing PKR autophosphorylation.[42] As PKR is a potent driver of many stress response pathways including translational shutdown, apoptosis, inflammation and metabolism, we hypothesized that PKR inhibition by the PKR-specific oxoindole/imidazole inhibitor C16 might rescue kidney injury in Tg26 mice. We administered C16 to Tg26 and wild type mice from age 6 to 12 weeks, at which time we evaluated kidney phenotype. C16-treated Tg26 mice had lower serum creatinine (**Figure 1A**) and albuminuria (**Figure 1B**) values compared to control Tg26 mice. Further, C16 treatment reduced the urinary kidney injury marker neutrophil gelatinase-associated lipocalin (NGAL) (**Figure 1C**).

There was an amelioration of glomerulosclerosis and of microtubular dilatation in C16-treated Tg26 observed histologically (**Figure 1D-F**). Histomorphological quantification confirmed that C16 treatment reduced glomerular injury, assessed as global glomerulosclerosis and segmental glomerulosclerosis (**Figure 1G, 1H)**, and fibrosis extent, quantified by Picrosirius Red staining (**Figure 1I-L)**.

*Combination of Single-nucleus RNA-seq and Bulk RNA-seq to profile transcriptomic changes in Tg26*

To investigate molecular mechanisms in Tg26 kidney and the effect of PKR inhibition, we conducted bulk RNA-seq of kidney cortex from the four groups (WT, WT treated with C16, Tg26, and Tg26 treated with C16; n=3 each) and single-nucleus RNA-seq of kidney cortex from

three samples (WT, Tg26, and Tg26 treated with C16; n=1 each) and of one sample of glomeruli from Tg26 mouse to enrich for glomerular cells (**Figure 2A**). Bulk RNA-seq data clustered well by treatment groups in a PCA plot (**Figure 2B**). Single-nucleus RNA-seq profiled a total of 30563 nuclei. Using Seurat's resolution parameter value of 0.6, we identified 23 cell clusters including a novel cell type (PT-Mito, proximal tubule cell cluster with a higher expression level of mitochondrial genes) as shown in UMAP (**Figure 2C, Supplemental Figure 1A**). Marker genes for each cluster used for annotation are shown in **Figure 2D**. Taking advantage of unbiased clustering in single-nucleus RNA-seq, we profiled relative cell numbers in each mouse kidney sample (**Figure 2E**, **Supplemental Figure 2**). The gene encoding PKR, *Eif2ak2*, was expressed globally in both glomeruli and tubular segments (**Supplemental Figure 1B**).

*Downregulation of mitochondrial genes in Tg26 kidneys*

GSEA results of bulk RNA-seq showed that mitochondrial related pathways were the most downregulated pathways in Tg26 mice when compared with WT mice, suggesting that mitochondrial gene transcription was significantly downregulated (**Figure 3A).** Specific mitochondrial gene expression levels were analyzed (**Figure 3C**) and C16 treatment reversed the downregulation of these mitochondrial genes (**Figure 3B**). Western blot results were consistent with bulk RNA-seq results showing lower abundance of mitochondrial complex I and II in Tg26 kidney and rescued by C16 treatment (**Figure 3D, Supplemental Figure 2**). Transcription factor A, mitochondrial (TFAM) abundance in kidney and mitochondrial DNA copy numbers were also decreased in Tg26 mice, but C16 treatment did not restore these changes (**Supplemental Figure 3A-E**). These findings suggest that PKR inhibition by C16 rescued transcriptional downregulation of both nuclear encoded and mitochondrial encoded mitochondrial genes but the

rescue was not through mitochondrial DNA copy number regulation mechanisms. Single-nucleus RNA-seq and subsequent Ingenuity Pathway Analysis (IPA) showed that the majority of cell types, including mitochondrial proximal tubules (PT-Mito), PT-S1, injured PT (PT-Inj), and endothelial cells manifested global downregulation of mitochondrial genes in Tg26 kidneys and that this decline was rescued by C16 treatment (**Figure 3E**).

*Novel proximal tubular cell cluster with high mitochondrial gene expression*

Based on the unbiased clustering, we found a distinct proximal tubule cell cluster with a higher expression level of mitochondrial genes (PT-Mito) consisting of 3.1 - 4.5% of kidney cortex cells (**Figure 2E**). We analyzed the proximal tubular cell clusters and found top markers to distinguish each cluster **(Figure 4A)**. Based on UMAP, this PT-Mito cluster was in proximity to PT-S1 and proliferating PT (PT-Prolif.) (**Figure 2C**). To confirm the presence of cells giving rise to this cluster in kidney tissue, in situ hybridization (ISH) of mt-Co1 and mt-Atp6 were performed. We observed transcripts inside some of nuclei and putative PT-Mito segments with high expression of these genes (**Figure 4B, 4C**). As this cluster was observed in both WT and Tg26 kidney in similar ratio, this new cluster could be a conserved tubular cell cluster never reported because of mitochondrial gene filtering criteria implemented in single-nucleus RNA-seq studies. IPA canonical pathway analysis of snRNA-seq data showed that the mitochondrial dysfunction was the most dysregulated in this PT-Mito cluster in Tg26 mice with a Z-score of -7.076 (**Figure 4D**). These data suggested that mitochondrial dysfunction represents a prominent mechanistic pathway that was dysregulated in majority of cell clusters in Tg26 mice, and that mitochondrial dysfunction was most pronounced in the PT-Mito cluster.

*Proximal tubular cells with injury and proliferation markers were more pronounced in Tg26*.

We identified one proximal tubular cell cluster enriched for injury markers (PT-Inj), which was increased in cell number and percentage in Tg26 sample when compared with WT mice and C16 treated-Tg26 mice. The gene expression profile of this cluster is comparable to previously reported mouse models of acute kidney injury (AKI)[38] and fibrosis.[43] Pseudotime analysis showed that injured proximal tubular epithelial cells likely originated from PT-S1 and PT-S2 segments, suggesting proximal tubular damage in Tg26 mouse kidneys (**Figure 4E, 4F**).

Differential gene expression analysis and IPA upstream analysis of bulk RNA-seq data from Tg26 and wild type mouse kidneys showed activation of the PKR pathway (**Figure 4G**). The per cluster upstream analysis of snRNA-seq data showed the highest activation of the PKR pathway for PT-Inj (**Figure 4H**). We further identified a proximal tubular cell cluster that displayed signs of cell proliferation (PT-Prolif), with high expression of *Top2a* and *Mki67* (**Figure 2D, 4A**). Cell cycle dysregulation is one of the main pathophysiological features of HIVAN and, corresponding to that, the PT-Prolif cluster had a higher cell number in the Tg26 kidney sample (**Figure 2E**). We also examined expression of cell cycle specific genes in S phase[44] and confirmed that the PT-Prolif cluster had the highest score of S phase transcripts among all clusters, especially in Tg26 tissue (**Supplemental Figure 3F**). Interestingly, we did not find a consistent change in the cell cycle phase scores in other clusters from the Tg26 sample.

*PKR inhibition rescued Stat3 activation in Tg26*

PKR inhibition, acting to reduce inflammatory pathway activation, may influence other important mediators of HIVAN pathophysiology. To identify possible intermediate factors, we used upstream analysis of IPA to find another mediator. We compared C16 treated WT vs WT, Tg26 vs WT, and C16 treated Tg26 vs Tg26, and applied differential gene expression analysis. All genes with multiple-testing adjusted p-value < 0.05 were included in the upstream analysis. An activated Z-score were calculated for each possible upstream regulator. Candidate transcription factors were sorted in the order of triple Z-score, which was calculated by multiplying of three Z-scores (**Supplemental Figure 4**).

Stat3 and representative examples of Stat3-regulated gene expressions profiles are shown for each tissue comparison (**Figure 5A, 5B**). Interestingly, Stat3 was the most activated upstream regulator, and is a well-characterized transcriptional regulator in kidney disease, including in the Tg26 mouse model.[19] We confirmed Stat3 activation through phosphorylation by Western blot showing phosphorylation (**Figure 5C, 5D**) and immunohistochemistry (**Figure 5E-G**). These data suggest that PKR inhibition may be therapeutic for Tg26 kidneys, promoting deactivation of Stat3 and downstream inflammatory pathways. Based on single-nucleus RNA-seq and IPA upstream analysis, we confirmed that Stat3 was activated in the majority of cell types in Tg26 and especially in PT-Inj (**Figure 5H**). As Stat3 is reported to suppress mitochondrial gene expression, Stat3 may also be important mitochondrial regulator in the pathogenesis of HIVAN.

*PKR inhibition restored reduced mitochondrial respiration capacity in Tg26*

Data shown above indicated that mitochondrial gene transcription was inhibited in the kidney cortex of Tg26 mice and was rescued by PKR inhibition. To investigate mitochondrial functions in kidney, we prepared enriched glomerular and proximal tubular cell tissue extracts. Glomeruli from Tg26 mice were tested for mitochondrial respiration capacity using the Seahorse extracellular flux analyzer. The results showed reduced maximum respiration and spare respiratory capacities in Tg26 (**Figure 6A-C**). Reduced respiratory capacities in Tg26 were rescued by C16 treatment, suggesting PKR inhibition restored reduced mitochondrial respiration in Tg26. Similarly, proximal tubular cells also showed less maximum respiration and spare respiratory capacity in Tg26 mice compared to wild type mice (**Figure 6D-F**) and were also rescued by C16 treatment. Thus, PKR inhibition rescues mitochondrial dysfunction in both glomerular and proximal tubular cells.

*Podocytes in Tg26 showed high HIV-1 genes expression with podocyte loss*

Even though the Tg26 mouse model is a well-characterized model of HIVAN, expression levels of each of the HIV-1 genes in kidney cells had not been reported. Taking advantage of single-nucleus RNA-seq, we annotated each HIV-1 gene with the aim to quantify HIV-1 gene expression at single cell resolution (**Figure 7A**). HIV-1 genes were expressed at highest levels in podocytes among all kidney cells, suggesting HIV-1 gene expression injures podocytes. HIV-1 gene expression data from this study agrees with the current understanding that *vpr* and *nef* are the main contributors to the pathogenesis of HIVAN. Absolute podocyte loss in Tg26, and podocyte recovery with C16, were also confirmed by p57 staining and podocyte estimation using the podometric analysis implemented in PodoCount (**Figure 7B-E**).

*Podocytes in Tg26 showed dedifferentiation and dysregulation of cytoskeleton related pathways*

Since podocytes in Tg26 mice expressed the HIV-1 genes *vpr* and *nef*, we investigated pathways that were dysregulated in podocytes in these mice. The yield of podocytes from kidney cortex samples was relatively low and, therefore, we used snRNA-seq data from isolated glomeruli from Tg26, which showed an enrichment in podocytes. Pseudotime analysis of these data showed a progression in transcripts from wild type podocytes to the majority of Tg26 podocytes (**Figure 7F**). Differential expression analysis and IPA canonical pathway analysis showed that RhoA and cGMP-related cytoskeleton formation pathways were activated in Tg26 (**Figure 7G**).

Those findings are consistent with previous reports and a common conceptual model in which podocyte dedifferentiation starts with cytoskeletal changes and progresses to cell detachment of the glomerular tuft.[45-47] We confirmed dedifferentiation of podocytes in Tg26 mice by showing down-regulation of podocyte markers and reversal or prevention of this in Tg26 treated with C16 (**Figure 7H**), which was demonstrated histologically by p57 staining (**Figure 7B-D**). We also found *Ccn2* (encoding cellular communication network factor 2), an epithelial–mesenchymal transition (EMT) marker, expressed in Tg26 podocytes. This is consistent with the signatures that we previously reported in a urinary single-cell study of human FSGS patients.[48] We also observed upregulation of *Rbfox1* as candidate disease marker in Tg26 podocytes (**Figure 7H**). Integrin subunits *Itga4* and *Itga1* and *Tgfb2* were also upregulated in Tg26 podocytes indicating activation of cell adhesion and pro-fibrotic processes (**Figure 7H**).

*Tg26 kidney cells showed active cell-cell interaction*

To investigate the pathologic cell-cell interactions in Tg26 kidney and the ameliorative effect of PKR inhibition, we performed cell-cell interaction analysis using the snRNA-seq data. The expression heatmap suggested changes in cell-cell interaction in each sample at the resolution of each identified cell cluster (**Supplemental Figure 5A-C**). We sought candidate cell types that contribute to Tg26 pathology and found candidate ligand-receptor pairs (**Figure 8A-C)**. For example, PDGF-D (platelet derived growth factor D), one of the markers of PT-Inj, was found to be upregulated in PT-Inj in Tg26 **(Figure 8D)** was interacting with PDGFR-B in fibroblast, and immunohistochemistry demonstrated the presence of PDGF-D in the vicinity of dilated tubular cells (**Figure 8E, 8F**). As PDGF-D is known to be induced by STAT3, we thereby identified a potential fibrogenesis pathway triggered by PKR activation in PT-Inj. In Tg26 mice, SPP1 (osteopontin)-a4b1 complex interaction was observed between endothelial cells, mesangial cells and podocytes. TGF- β pathways were also activated between glomerular and tubular cells.

## Discussion

The finding reported here highlight the role of PKR activation in the Tg26 HIVAN mouse model and show mitochondrial dysfunction to be one of the most dysregulated pathways by applying a combined analysis of single-nucleus RNA-seq and bulk RNA-seq data. Single-nucleus RNA-sequencing of Tg26 kidney cortex identified a novel mitochondrial gene-enriched proximal tubular cell population (PT-Mito). This cell population had been previously unrecognized, likely due to filtering criteria routinely employed to reduced mitochondrial genome-encoded transcript levels in single-cell/single nucleus datasets. Although it has been well established that mitochondrial transcript percentage captured can be a good criterion to filter out stressed cells from the analysis in single-cell RNA-seq, single-nucleus RNA-seq does not have to use the same quality control criteria because mitochondrial gene percentage is generally low following the nuclei purification step. Here, most nuclei captured had mitochondrial transcripts levels of < 1% of the total transcripts captured. Therefore, we did not filter out mitochondrial transcripts entirely from the analysis but followed the 20% mitochondrial transcript value cutoff criteria to filter nuclei as reported by Slyper et al.[49]

We further confirmed the presence of mitochondrial transcripts identified in the single-nuclei analysis in nuclei of corresponding tissue samples by ISH. A relative high abundance of mitochondrial transcripts in the PT-Mito cluster may indicate existence of mitochondrial transcripts transported into nuclei. This PT-Mito cluster might have remained undetected because of the similarity of its transcripts with that of other PTs and the lack of specific markers. Considering the high mitochondrial gene expression levels and corresponding pathway dysregulation in Tg26 mice, this PT-Mito cluster may harbor be the most metabolically active and with that also highly vulnerable cell types in kidney proximal tubules. Nevertheless,

considering the downregulation of both nuclear and mitochondrial encoded genes involved in oxidative phosphorylation; mitochondrial dysfunction likely plays a major role in the pathology of HIVAN. Mitochondrial dysfunction in Tg26 mouse kidney and myocytes has been previously reported.[24,50] It is likely that PKR is one of several components that contributes to mitochondrial dysfunction in HIVAN. This warrants the investigation of other causes of mitochondrial dysfunction in HIVAN with the aim to shed further light on injury pathways and to assess feasibility of treatment options.

A second novel finding resulted from investigating HIV-1 gene expression in the Tg26 model. In this transgenic mouse, transcripts for all transgene-encoded HIV-1 genes were detected in all cell types, albeit some at low expression levels. This included transcripts for *nef* and *vpr* that are, according to our current understanding, the main contributors to HIVAN.[51,52] Interestingly, podocytes showed the highest levels of retroviral gene expression, which is consistent with the prominent phenotype observed in podocytes. Although it is unclear why podocytes expressed the highest levels of HIV genes in Tg26 mice, this finding suggests a shared mechanism in virus related nephropathies that exhibit podocyte damage.

Further, we identified putative, activated PKR - STAT3 - PDGF-D - PDGFR-B pathways in injured proximal tubules. PDGF-D and PDGFR-B have been reported to contribute to fibrosis in glomeruli and tubules[53,54]. Inhibiting this prominent pathway may offer an avenue to reduce kidney injury in HIVAN. Further validation will be needed to confirm if this mechanism observed in Tg26 mice is shared with that in human HIVAN.

In conclusion, by combining single-nucleus and bulk RNA-seq analysis we identified mitochondrial dysfunction as the central mechanism for proximal tubule injury in the Tg26 HIVAN mouse model, a process that was largely reversed by treatment of the mice with the PKR

inhibitor C16. Further research into the HIVAN driven mitochondrial dysfunction may lead to targeted therapy opportunities.

## Figure Legends

**Figure. 1 PKR inhibition by C16 ameliorates Tg26 mice kidney phenotype.**

(**A-C**) plasma creatinine (mg/dL), urinary albumin-to-creatinine ratio (mg/g creatinine), urinary NGAL-to-creatinine ratio (ng/g creatinine). (**D-F**) Representative PAS staining images of WT, Tg26 and C16 treated Tg26 kidney. (**G, H**) Quantitative analysis of glomeruli for segmental scaring, global sclerosis. (**I, K**) Representative Picrosirius Red-staining images of WT, Tg26 and C16 treated Tg26 kidney. (**L**) Quantitative analysis of Picrosirius Red-staining area. (One-way ANOVA (**A-C**), t-test (**G, H, L**); *, $P<0.05$; **, $P<0.01$; scale bars are 50 μm)

**Figure. 2 Overview of bulk mRNA-seq and single-nucleus RNA-seq experiments.** (**A**) Workflow of bulk mRNA-seq and single-nucleus RNA-seq experiments. (**B**) Principal component analysis plot of mRNA-seq results. (**C**) UMAP plot of single-nuclear RNA-seq data from 4 samples, 30563 nuclei, showing 23 clusters. (**D**) Dot plot of 23 marker genes characteristic for each cluster. (**E**) Ratio of nuclei grouped to each cluster by each sample.

**Figure. 3 Oxidative phosphorylation genes are downregulated in Tg26 and downregulation is reversed by PKR inhibition using C16.** (**A**) Enrichment plot of oxidative phosphorylation pathway based on bulk mRNA-seq comparing Tg26 and WT. (**B**) Enrichment plot of oxidative phosphorylation pathway based on bulk mRNA-seq comparing C16 treated Tg26 and Tg26. (**C**) Heatmap of expressed genes in oxidative phosphorylation pathway (n=123) based on bulk mRNA-seq. (**D**) Western blot probed against mitochondrial subunits CI through CIV and VDAC. (**E**) Dot plot showing expression of oxidative phosphorylation pathway genes in PT-Mito, PT-S1, PT-Inj, Endo, Fibroblast cluster by snRNA-seq.

**Figure. 4 PT-Mito and PT-Inj cluster characterization.** (**A**) Dot plot showing top 5 marker genes in each PT clusters (PT-S1, PT-S1/S2, PT-S2, PT-S3, PT-Prolif, PT-Inj, PT-Mito). (**B, C**) *In situ* Hybridization of mt-Co1 and mt-Atp6 showing respective signals inside nuclei. (Scale bars are 50 μm) (**D**) Activation Z-score of oxidative phosphorylation pathway by IPA in each cluster comparing Tg26 vs WT. (**E**) Trajectory analysis results including PT-S1, PT-Mito, PT-Inj, PT-Prolif from WT and Tg26. (**F**) Trajectory analysis results including PT-S2 and PT-Inj from WT and Tg26. (**G**) PKR downstream pathway mapping by IPA comparing Tg26 vs WT by bulk mRNA-seq data. (**H**) Activation Z-score of PKR pathway by IPA in each cluster comparing Tg26 vs WT.

**Figure. 5 STAT3 activation downstream of PKR.** (**A, B**) Mapping of STAT3 regulating genes comparing Tg26 vs WT (Z-score 6.286), Tg26 C16 vs Tg26 (Z-score -3.182) by bulk mRNA-seq. Red color indicates upregulation and green color indicates downregulation with log2-fold change, p-value, and adjusted p-value (FDR). Solid line indicates known positive regulation, dotted line indicates known negative regulation. (**C**) Representative immunoblotting of phospho-STAT3, STAT3 and β-ACTIN. (**D**) Quantitative results of phospho-STAT3/STAT3 by immunoblotting. (One-way ANOVA; *, $P<0.05$) (**E-G**) Immunohistochemistry of kidneys by phospho-STAT3 staining. (Scale bars are 50 μm) (**H**) STAT3 activation Z-score by IPA comparing Tg26 vs WT in each cluster by snRNA-seq.

**Figure. 6 PKR inhibition with C16 reverses mitochondrial dysfunction in Tg26 glomeruli and proximal tubules.** (**A**) Oxygen consumption rate (OCR) measurements with cell mito stress

test using extracted glomeruli from WT, Tg26, C16 Tg26 kidney. (**B**) Maximum respiration rate calculated by OCR measurements of glomeruli. (**C**) Spare respiratory capacity calculated by OCR measurements of glomeruli. (**D**) Oxygen consumption rate (OCR) measurements with cell mito stress test using extracted proximal tubules from WT, Tg26, C16 Tg26 kidney. (**E**) Maximum respiration rate calculated by OCR measurements of proximal tubules. (**F**) Spare respiratory capacity calculated by OCR measurements of proximal tubules. (One-way ANOVA; *, $P<0.05$; **, $P<0.01$)

**Figure. 7 HIV-1 gene expression causes Tg26 podocytes dedifferentiation.** (**A**) Dot plot showing HIV-1 gene expression levels in each cluster detected by snRNA-seq. (**B-D**) p57 staining of kidney showing podocyte loss and dedifferentiation. (Scale bars are 50 μm) (**E**) Podocount analysis showed podocyte loss in Tg26 and was rescued by C16. (One-way ANOVA; *, $P<0.05$; ***, $P<0.001$) (**F**) Trajectory analysis of podocytes by snRNA-seq data from WT, Tg26 glom samples. (**G**) Canonical pathway analysis results by IPA comparing Tg26 vs WT using snRNA-seq data from podocyte cluster. (**H**) Dot plot showing podocyte marker genes and representative differentially expressed genes in Tg26 podocytes by snRNA-seq.

**Figure. 8 Cell-cell interaction analysis shows activated ligand-receptor interaction: PDGF-D-PDGFR-B pathway in Tg26.** (**A-C**) Dot plots depicting results from cell-cell interaction analysis of WT, Tg26, C16 Tg26 snRNA-seq data. (**D**) Violin plots showing Pdgfd expression level in PT-Inj cluster. (**E, F**) Immunohistochemistry of kidneys by PDGF-D staining. (Scale bars are 50 μm)

## Author Contributions

TY, KO, JBK conceived the study design. TY conducted mouse experiments with support by SS. TY analyzed bulk RNA-seq data. TY and YY conducted single-nuclear RNA-seq capture. TY and KZL analyzed single-nuclear RNA-seq data. YZ and CAW supported sequencing at FNLCR/NCI. AZR assessed pathological quantification. BS, TY, VT and PS conducted podocyte morphometry. KM, BJ, XW conducted OXPHOS complex Western blot. TY, JBK drafted the manuscript and all the authors contributed for edits. The order of the co-first authors was based on when they started on the project and the relative contribution to the authoring of the original version of the manuscript.

## Acknowledgement

We thank the Sequencing Facility and Bioinformatics Group (Frederick National Laboratory for Cancer Research (FNLCR), NCI, NIH) for sequencing and informatics support, Drs. Joon-Yong Chung and Stephen M. Hewitt (NCI/NIH) for whole slide scanning, Maria Campos (NEI/NIH) for pathological service, Dr. Daria Ilatovskaya (Medical University of South Carolina) for suggestion of Seahorse assay, and Drs. Mark A. Knepper (NHLBI, NIH) and Gregory G. Germino (NIDDK, NIH) for scientific suggestions and supports, Dr. Jurgen Heymann for critical manuscript review. This work utilized the computational resources of the NIH HPC Biowulf cluster. (http://hpc.nih.gov) The content of this publication does not necessarily reflect the views or policies of the Department of Health and Human Services, nor does mention of trade names, commercial products, or organizations imply endorsement by the U.S. Government.

**Funding**

This project has been funded in part with federal funds from the National Cancer Institute, National Institutes of Health, under contract 75N91019D00024. This Research was supported by the Intramural Research Program of the NIH, including the National Cancer Institute, Center for Cancer Research and the NIDDK.

**Data Availability**

Original data files and count tables have been deposited in GEO (GSE205060). Other data are available from the authors upon request.

## References


1. Fauci AS. NIH Statement on World AIDS Day. Accessed 12/2, 2021. https://www.niaid.nih.gov/news-events/nih-statement-world-aids-day-2021
2. Prevention CfDCa. HIV Surveillance Report, 2019; vol.32. Accessed 11/29, 2021. http://www.cdc.gov/hiv/library/reports/hiv-surveillance.html
3. Dwyer-Lindgren L, Cork MA, Sligar A, et al. Mapping HIV prevalence in sub-Saharan Africa between 2000 and 2017. *Nature*. Jun 2019;570(7760):189-193. doi:10.1038/s41586-019-1200-9
4. Palau L, Menez S, Rodriguez-Sanchez J, et al. HIV-associated nephropathy: links, risks and management. *HIV AIDS (Auckl)*. 2018;10:73-81. doi:10.2147/HIV.S141978
5. Menez S, Hanouneh M, McMahon BA, Fine DM, Atta MG. Pharmacotherapy and treatment options for HIV-associated nephropathy. *Expert Opin Pharmacother*. Jan 2018;19(1):39-48. doi:10.1080/14656566.2017.1416099
6. Yahaya I, Uthman OA, Uthman MM. Interventions for HIV-associated nephropathy. *Cochrane Database Syst Rev*. Jan 31 2013;(1):CD007183. doi:10.1002/14651858.CD007183.pub3
7. Bruggeman LA, Dikman S, Meng C, Quaggin SE, Coffman TM, Klotman PE. Nephropathy in human immunodeficiency virus-1 transgenic mice is due to renal transgene expression. *J Clin Invest*. Jul 1 1997;100(1):84-92. doi:10.1172/JCI119525
8. Dickie P, Felser J, Eckhaus M, et al. HIV-associated nephropathy in transgenic mice expressing HIV-1 genes. *Virology*. Nov 1991;185(1):109-19. doi:10.1016/0042-6822(91)90759-5
9. Kopp JB, Klotman ME, Adler SH, et al. Progressive glomerulosclerosis and enhanced renal accumulation of basement membrane components in mice transgenic for human immunodeficiency virus type 1 genes. *Proc Natl Acad Sci U S A*. Mar 1 1992;89(5):1577-81. doi:10.1073/pnas.89.5.1577
10. Kumar D, Konkimalla S, Yadav A, et al. HIV-associated nephropathy: role of mammalian target of rapamycin pathway. *Am J Pathol*. Aug 2010;177(2):813-21. doi:10.2353/ajpath.2010.100131
11. Yadav A, Kumar D, Salhan D, et al. Sirolimus modulates HIVAN phenotype through inhibition of epithelial mesenchymal transition. *Exp Mol Pathol*. Aug 2012;93(1):173-81. doi:10.1016/j.yexmp.2012.04.021
12. Rai P, Plagov A, Lan X, et al. mTOR plays a critical role in p53-induced oxidative kidney cell injury in HIVAN. *Am J Physiol Renal Physiol*. Aug 1 2013;305(3):F343-54. doi:10.1152/ajprenal.00135.2013
13. Sharma M, Magenheimer LK, Home T, et al. Inhibition of Notch pathway attenuates the progression of human immunodeficiency virus-associated nephropathy. *Am J Physiol Renal Physiol*. Apr 15 2013;304(8):F1127-36. doi:10.1152/ajprenal.00475.2012
14. Puri RV, Yerrathota S, Home T, et al. Notch4 activation aggravates NF-kappaB-mediated inflammation in HIV-1-associated nephropathy. *Dis Model Mech*. Dec 17 2019;12(12)doi:10.1242/dmm.040642
15. Zhong Y, Chen EY, Liu R, et al. Renoprotective effect of combined inhibition of angiotensin-converting enzyme and histone deacetylase. *J Am Soc Nephrol*. Apr 2013;24(5):801-11. doi:10.1681/ASN.2012060590

16. Rai P, Lederman R, Haque S, et al. Renin angiotensin system modulates mTOR pathway through AT2R in HIVAN. *Exp Mol Pathol*. Jun 2014;96(3):431-7. doi:10.1016/j.yexmp.2014.04.004
17. Gherardi D, D'Agati V, Chu TH, et al. Reversal of collapsing glomerulopathy in mice with the cyclin-dependent kinase inhibitor CYC202. *J Am Soc Nephrol*. May 2004;15(5):1212-22. doi:10.1097/01.asn.0000124672.41036.f4
18. Wang X, Liu R, Zhang W, et al. Role of SIRT1 in HIV-associated kidney disease. *Am J Physiol Renal Physiol*. Aug 1 2020;319(2):F335-F344. doi:10.1152/ajprenal.00140.2020
19. Feng X, Lu TC, Chuang PY, et al. Reduction of Stat3 activity attenuates HIV-induced kidney injury. *J Am Soc Nephrol*. Oct 2009;20(10):2138-46. doi:10.1681/asn.2008080879
20. Gu L, Dai Y, Xu J, et al. Deletion of podocyte STAT3 mitigates the entire spectrum of HIV-1-associated nephropathy. *AIDS*. Apr 24 2013;27(7):1091-8. doi:10.1097/QAD.0b013e32835f1ea1
21. Ratnam KK, Feng X, Chuang PY, et al. Role of the retinoic acid receptor-α in HIV-associated nephropathy. *Kidney Int*. Mar 2011;79(6):624-634. doi:10.1038/ki.2010.470
22. Zhang G, Liu R, Zhong Y, et al. Down-regulation of NF-kappaB transcriptional activity in HIV-associated kidney disease by BRD4 inhibition. *J Biol Chem*. Aug 17 2012;287(34):28840-51. doi:10.1074/jbc.M112.359505
23. Haque S, Lan X, Wen H, et al. HIV Promotes NLRP3 Inflammasome Complex Activation in Murine HIV-Associated Nephropathy. *Am J Pathol*. Feb 2016;186(2):347-58. doi:10.1016/j.ajpath.2015.10.002
24. Bryant JL, Guda PR, Asemu G, et al. Glomerular mitochondrial changes in HIV associated renal injury. *Exp Mol Pathol*. Jun 2018;104(3):175-189. doi:10.1016/j.yexmp.2018.03.004
25. Katuri A, Bryant JL, Patel D, et al. HIVAN associated tubular pathology with reference to ER stress, mitochondrial changes, and autophagy. *Exp Mol Pathol*. Feb 2019;106:139-148. doi:10.1016/j.yexmp.2018.12.009
26. Jin Y, Ratnam K, Chuang PY, et al. A systems approach identifies HIPK2 as a key regulator of kidney fibrosis. *Nat Med*. Mar 11 2012;18(4):580-8. doi:10.1038/nm.2685
27. Liu R, Das B, Xiao W, et al. A Novel Inhibitor of Homeodomain Interacting Protein Kinase 2 Mitigates Kidney Fibrosis through Inhibition of the TGF-beta1/Smad3 Pathway. *J Am Soc Nephrol*. Jul 2017;28(7):2133-2143. doi:10.1681/ASN.2016080841
28. Xiao W, E J, Bao L, et al. Tubular HIPK2 is a key contributor to renal fibrosis. *JCI Insight*. Sep 3 2020;5(17)doi:10.1172/jci.insight.136004
29. Fan Y, Wei C, Xiao W, et al. Temporal profile of the renal transcriptome of HIV-1 transgenic mice during disease progression. *PLoS One*. 2014;9(3):e93019. doi:10.1371/journal.pone.0093019
30. Okamoto K, Rausch JW, Wakashin H, et al. APOL1 risk allele RNA contributes to renal toxicity by activating protein kinase R. *Commun Biol*. 2018;1:188. doi:10.1038/s42003-018-0188-2
31. Tronel C, Page G, Bodard S, Chalon S, Antier D. The specific PKR inhibitor C16 prevents apoptosis and IL-1beta production in an acute excitotoxic rat model with a neuroinflammatory component. *Neurochem Int*. Jan 2014;64:73-83. doi:10.1016/j.neuint.2013.10.012

32. Ingrand S, Barrier L, Lafay-Chebassier C, Fauconneau B, Page G, Hugon J. The oxindole/imidazole derivative C16 reduces in vivo brain PKR activation. *FEBS Lett*. Sep 18 2007;581(23):4473-8. doi:10.1016/j.febslet.2007.08.022
33. Kasembeli AN, Duarte R, Ramsay M, et al. APOL1 Risk Variants Are Strongly Associated with HIV-Associated Nephropathy in Black South Africans. *J Am Soc Nephrol*. Nov 2015;26(11):2882-90. doi:10.1681/asn.2014050469
34. Iwakura T, Zhao Z, Marschner JA, Devarapu SK, Yasuda H, Anders HJ. Dipeptidyl peptidase-4 inhibitor teneligliptin accelerates recovery from cisplatin-induced acute kidney injury by attenuating inflammation and promoting tubular regeneration. *Nephrol Dial Transplant*. Oct 1 2019;34(10):1669-1680. doi:10.1093/ndt/gfy397
35. Andargie TE, Tsuji N, Seifuddin F, et al. Cell-free DNA maps COVID-19 tissue injury and risk of death and can cause tissue injury. *JCI Insight*. Apr 8 2021;6(7)doi:10.1172/jci.insight.147610
36. Martin M. Cutadapt removes adapter sequences from high-throughput sequencing reads. next generation sequencing; small RNA; microRNA; adapter removal. *2011*. 2011-05-02 2011;17(1):3. doi:10.14806/ej.17.1.200
37. Kramer A, Green J, Pollard J, Jr., Tugendreich S. Causal analysis approaches in Ingenuity Pathway Analysis. *Bioinformatics*. Feb 15 2014;30(4):523-30. doi:10.1093/bioinformatics/btt703
38. Kirita Y, Wu H, Uchimura K, Wilson PC, Humphreys BD. Cell profiling of mouse acute kidney injury reveals conserved cellular responses to injury. *Proc Natl Acad Sci U S A*. Jul 7 2020;117(27):15874-15883. doi:10.1073/pnas.2005477117
39. Santo BA, Govind D, Daneshpajouhnejad P, et al. PodoCount: A Robust, Fully Automated, Whole-Slide Podocyte Quantification Tool. *Kidney International Reports*. 2022;7(6):1377-1392. doi:10.1016/j.ekir.2022.03.004
40. Kikuchi M, Wickman L, Hodgin JB, Wiggins RC. Podometrics as a potential clinical tool for glomerular disease management. Elsevier; 2015:245-255.
41. Venkatareddy M, Wang S, Yang Y, et al. Estimating podocyte number and density using a single histologic section. *Journal of the American Society of Nephrology*. 2014;25(5):1118-1129.
42. Carpick BW, Graziano V, Schneider D, Maitra RK, Lee X, Williams BR. Characterization of the solution complex between the interferon-induced, double-stranded RNA-activated protein kinase and HIV-I trans-activating region RNA. *J Biol Chem*. Apr 4 1997;272(14):9510-6. doi:10.1074/jbc.272.14.9510
43. Lu YA, Liao CT, Raybould R, et al. Single-Nucleus RNA Sequencing Identifies New Classes of Proximal Tubular Epithelial Cells in Kidney Fibrosis. *J Am Soc Nephrol*. Oct 2021;32(10):2501-2516. doi:10.1681/asn.2020081143
44. Tirosh I, Izar B, Prakadan SM, et al. Dissecting the multicellular ecosystem of metastatic melanoma by single-cell RNA-seq. *Science*. Apr 8 2016;352(6282):189-96. doi:10.1126/science.aad0501
45. Lu TC, He JC, Wang ZH, et al. HIV-1 Nef disrupts the podocyte actin cytoskeleton by interacting with diaphanous interacting protein. *J Biol Chem*. Mar 28 2008;283(13):8173-82. doi:10.1074/jbc.M708920200
46. Husain M, D'Agati VD, He JC, Klotman ME, Klotman PE. HIV-1 Nef induces dedifferentiation of podocytes in vivo: a characteristic feature of HIVAN. *Aids*. Nov 18 2005;19(17):1975-80. doi:10.1097/01.aids.0000191918.42110.27

47. Sunamoto M, Husain M, He JC, Schwartz EJ, Klotman PE. Critical role for Nef in HIV-1-induced podocyte dedifferentiation. *Kidney Int*. Nov 2003;64(5):1695-701. doi:10.1046/j.1523-1755.2003.00283.x
48. Latt KZ, Heymann J, Jessee JH, et al. Urine Single-Cell RNA Sequencing in Focal Segmental Glomerulosclerosis Reveals Inflammatory Signatures. *Kidney Int Rep*. Feb 2022;7(2):289-304. doi:10.1016/j.ekir.2021.11.005
49. Slyper M, Porter CBM, Ashenberg O, et al. A single-cell and single-nucleus RNA-Seq toolbox for fresh and frozen human tumors. *Nat Med*. May 2020;26(5):792-802. doi:10.1038/s41591-020-0844-1
50. Cheung JY, Gordon J, Wang J, et al. Mitochondrial dysfunction in human immunodeficiency virus-1 transgenic mouse cardiac myocytes. *J Cell Physiol*. Apr 2019;234(4):4432-4444. doi:10.1002/jcp.27232
51. Zuo Y, Matsusaka T, Zhong J, et al. HIV-1 genes vpr and nef synergistically damage podocytes, leading to glomerulosclerosis. *J Am Soc Nephrol*. Oct 2006;17(10):2832-43. doi:10.1681/ASN.2005080878
52. Rednor SJ, Ross MJ. Molecular Mechanisms of Injury in HIV-Associated Nephropathy. *Front Med (Lausanne)*. 2018;5:177. doi:10.3389/fmed.2018.00177
53. Kok HM, Falke LL, Goldschmeding R, Nguyen TQ. Targeting CTGF, EGF and PDGF pathways to prevent progression of kidney disease. *Nat Rev Nephrol*. Dec 2014;10(12):700-11. doi:10.1038/nrneph.2014.184
54. Buhl EM, Djudjaj S, Klinkhammer BM, et al. Dysregulated mesenchymal PDGFR-beta drives kidney fibrosis. *EMBO Mol Med*. Mar 6 2020;12(3):e11021. doi:10.15252/emmm.201911021

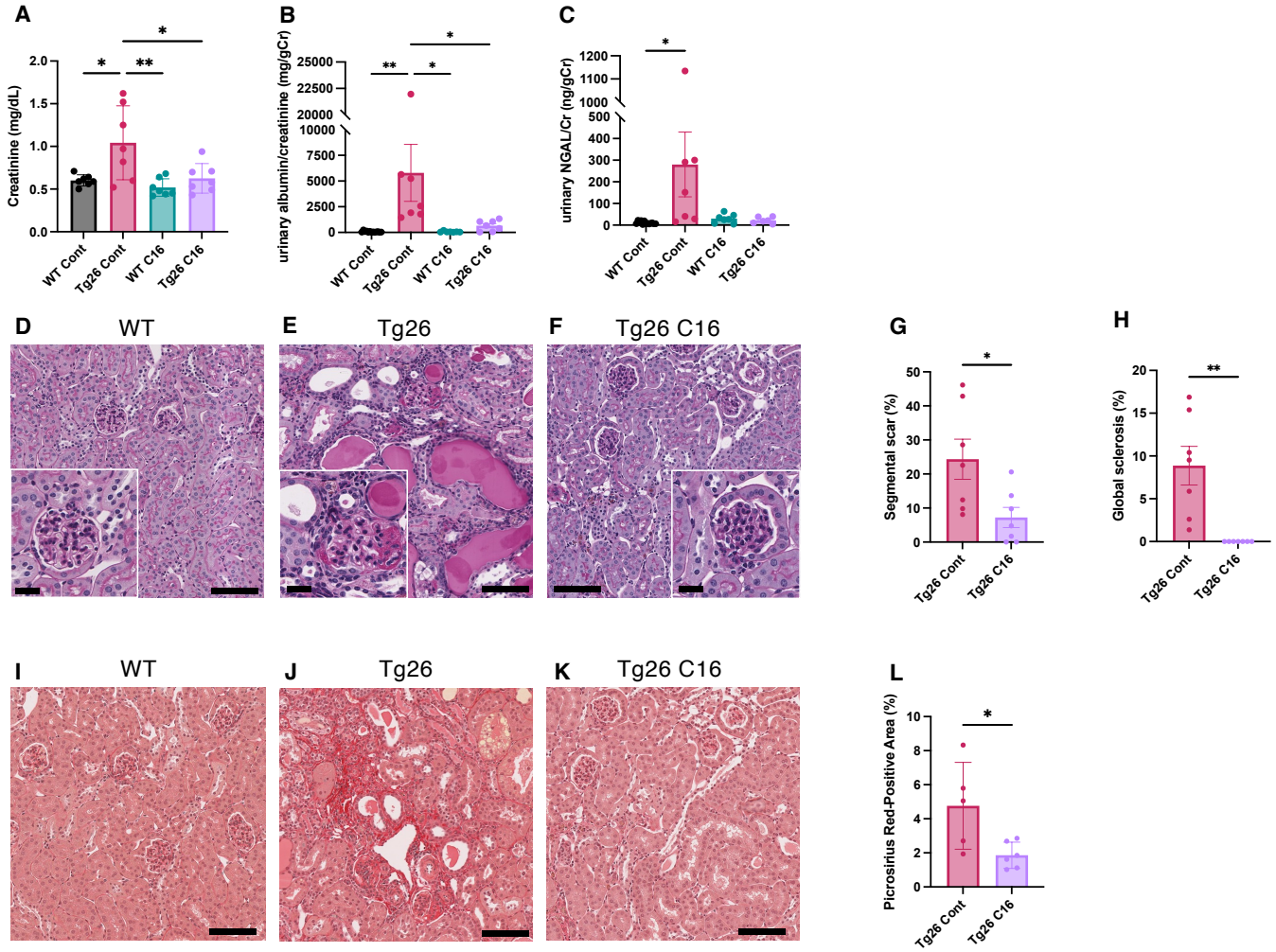


**Figure. 1 PKR inhibition by C16 ameliorates Tg26 mice kidney phenotype.**
(**A-C**) plasma creatinine (mg/dL), urinary albumin-to-creatinine ratio (mg/g creatinine), urinary NGAL-to-creatinine ratio (ng/g creatinine). (**D-F**) Representative PAS staining images of WT, Tg26 and C16 treated Tg26 kidney. (**G, H**) Quantitative analysis of glomeruli for segmental scaring, global sclerosis. (**I, K**) Representative Picrosirius Red-staining images of WT, Tg26 and C16 treated Tg26 kidney. (**L**) Quantitative analysis of Picrosirius Red-staining area. (One-way ANOVA (**A-C**), t-test (**G, H, L**);
*, P<0.05; **, P<0.01; scale bars are 50 µm)

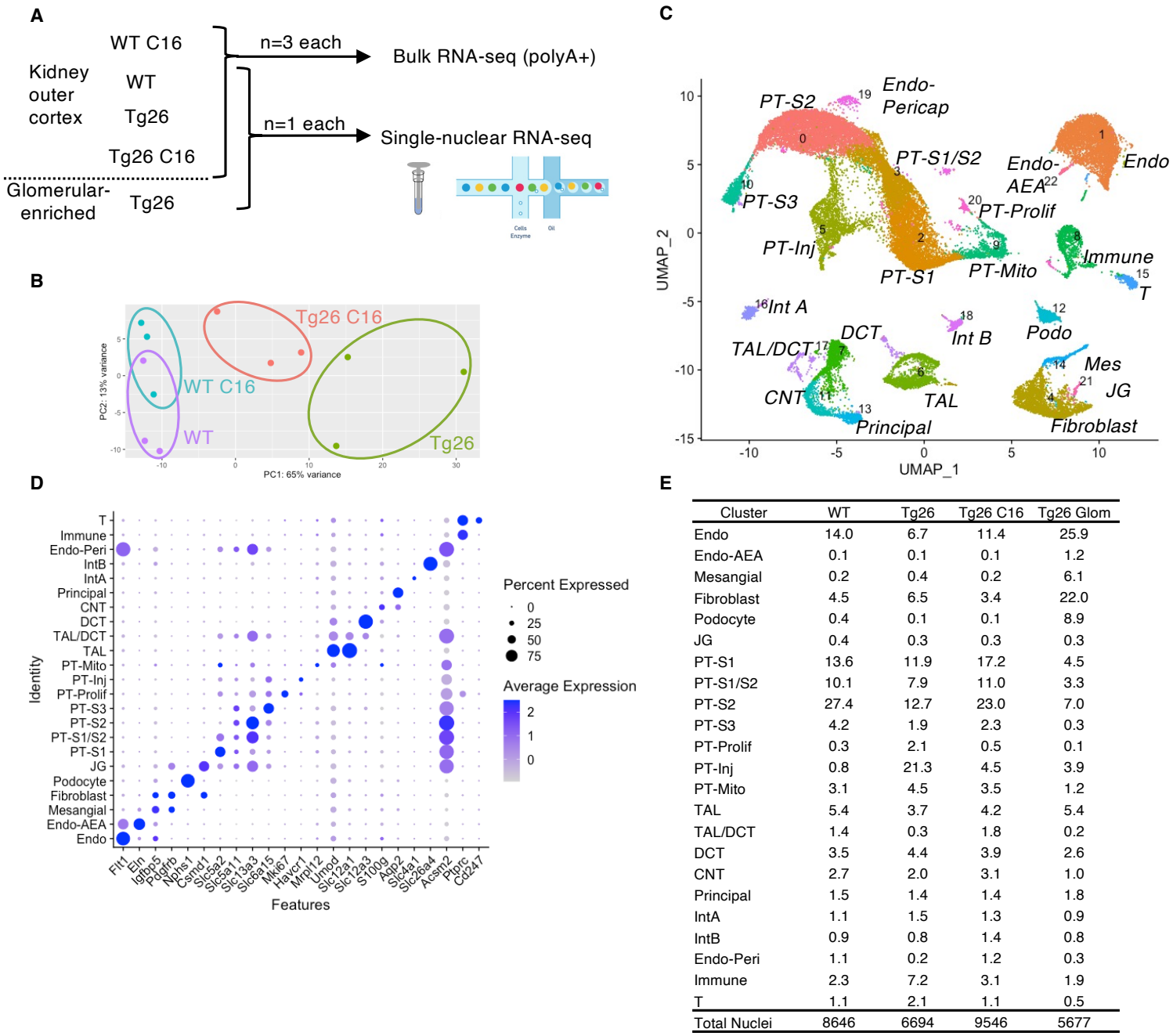


| Cluster | WT | Tg26 | Tg26 C16 | Tg26 Glom |
|---|---|---|---|---|
| Endo | 14.0 | 6.7 | 11.4 | 25.9 |
| Endo-AEA | 0.1 | 0.1 | 0.1 | 1.2 |
| Mesangial | 0.2 | 0.4 | 0.2 | 6.1 |
| Fibroblast | 4.5 | 6.5 | 3.4 | 22.0 |
| Podocyte | 0.4 | 0.1 | 0.1 | 8.9 |
| JG | 0.4 | 0.3 | 0.3 | 0.3 |
| PT-S1 | 13.6 | 11.9 | 17.2 | 4.5 |
| PT-S1/S2 | 10.1 | 7.9 | 11.0 | 3.3 |
| PT-S2 | 27.4 | 12.7 | 23.0 | 7.0 |
| PT-S3 | 4.2 | 1.9 | 2.3 | 0.3 |
| PT-Prolif | 0.3 | 2.1 | 0.5 | 0.1 |
| PT-Inj | 0.8 | 21.3 | 4.5 | 3.9 |
| PT-Mito | 3.1 | 4.5 | 3.5 | 1.2 |
| TAL | 5.4 | 3.7 | 4.2 | 5.4 |
| TAL/DCT | 1.4 | 0.3 | 1.8 | 0.2 |
| DCT | 3.5 | 4.4 | 3.9 | 2.6 |
| CNT | 2.7 | 2.0 | 3.1 | 1.0 |
| Principal | 1.5 | 1.4 | 1.4 | 1.8 |
| IntA | 1.1 | 1.5 | 1.3 | 0.9 |
| IntB | 0.9 | 0.8 | 1.4 | 0.8 |
| Endo-Peri | 1.1 | 0.2 | 1.2 | 0.3 |
| Immune | 2.3 | 7.2 | 3.1 | 1.9 |
| T | 1.1 | 2.1 | 1.1 | 0.5 |
| Total Nuclei | 8646 | 6694 | 9546 | 5677 |

**Figure. 2 Overview of bulk mRNA-seq and single-nucleus RNA-seq experiments.**
(**A**) Workflow of bulk mRNA-seq and single-nucleus RNA-seq experiments. (**B**) Principal component analysis plot of mRNA-seq results.
(**C**) UMAP plot of single-nuclear RNA-seq data from 4 samples, 30563 nuclei, showing 23 clusters.
(**D**) Dot plot of 23 marker genes characteristic for each cluster. (**E**) Ratio of nuclei grouped to each cluster by each sample

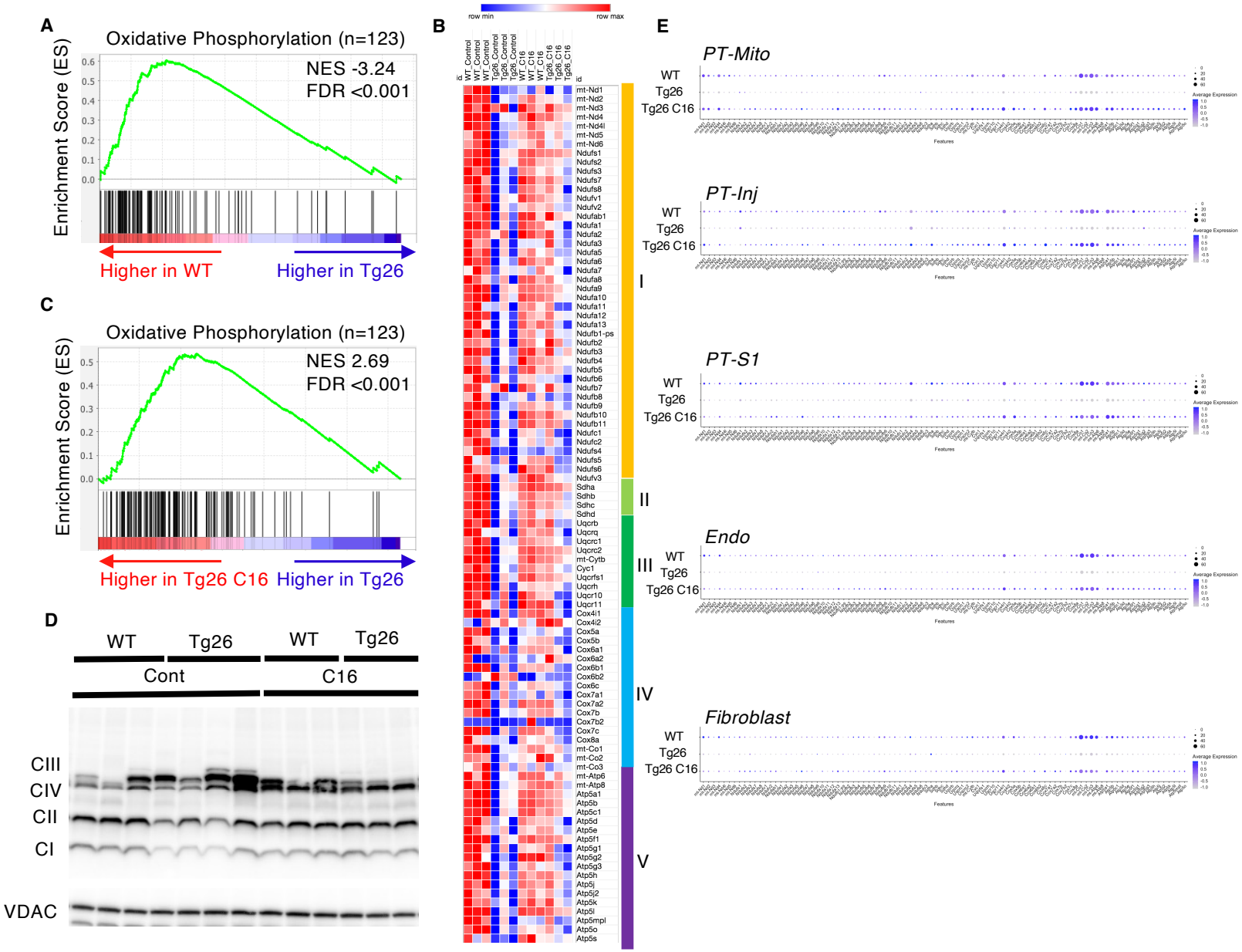


**Figure. 3 Oxidative phosphorylation genes are downregulated in Tg26 and downregulation is reversed by PKR inhibition using C16.**
(**A**) Enrichment plot of oxidative phosphorylation pathway based on bulk mRNA-seq comparing Tg26 and WT.
(**B**) Enrichment plot of oxidative phosphorylation pathway based on bulk mRNA-seq comparing C16 treated Tg26 and Tg26.
(**C**) Heatmap of expressed genes in oxidative phosphorylation pathway (n=123) based on bulk mRNA-seq.
(**D**) Western blot probed against mitochondrial subunits CI through CIV and VDAC.
(**E**) Dot plot showing expression of oxidative phosphorylation pathway genes in PT-Mito, PT-S1, PT-Inj, Endo, Fibroblast cluster by snRNA-seq.

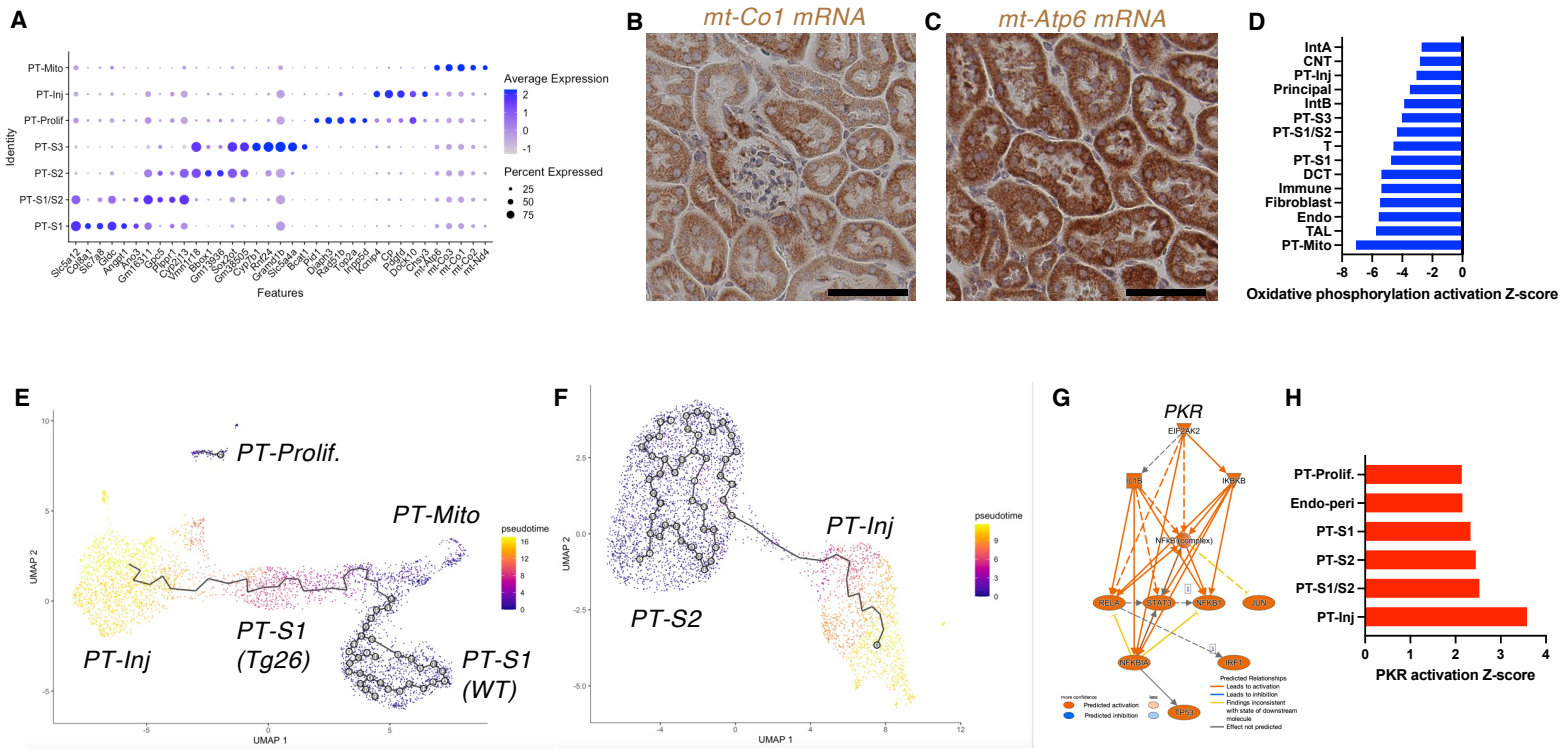


**Figure. 4 PT-Mito and PT-Inj cluster characterization.**

(**A**) Dot plot showing top 5 marker genes in each PT clusters (PT-S1, PT-S1/S2, PT-S2, PT-S3, PT-Prolif, PT-Inj, PT-Mito).

(**B, C**) *In situ* Hybridization of mt-Co1 and mt-Atp6 showing respective signals inside nuclei. (Scale bars are 50 µm)

(**D**) Activation Z-score of oxidative phosphorylation pathway by IPA in each cluster comparing Tg26 vs WT.

(**E**) Trajectory analysis results including PT-S1, PT-Mito, PT-Inj, PT-Prolif from WT and Tg26. (**F**) Trajectory analysis results including PT-S2 and PT-Inj from WT and Tg26. (**G**) PKR downstream pathway mapping by IPA comparing Tg26 vs WT by bulk mRNA-seq data.

(**H**) Activation Z-score of PKR pathway by IPA in each cluster comparing Tg26 vs WT.

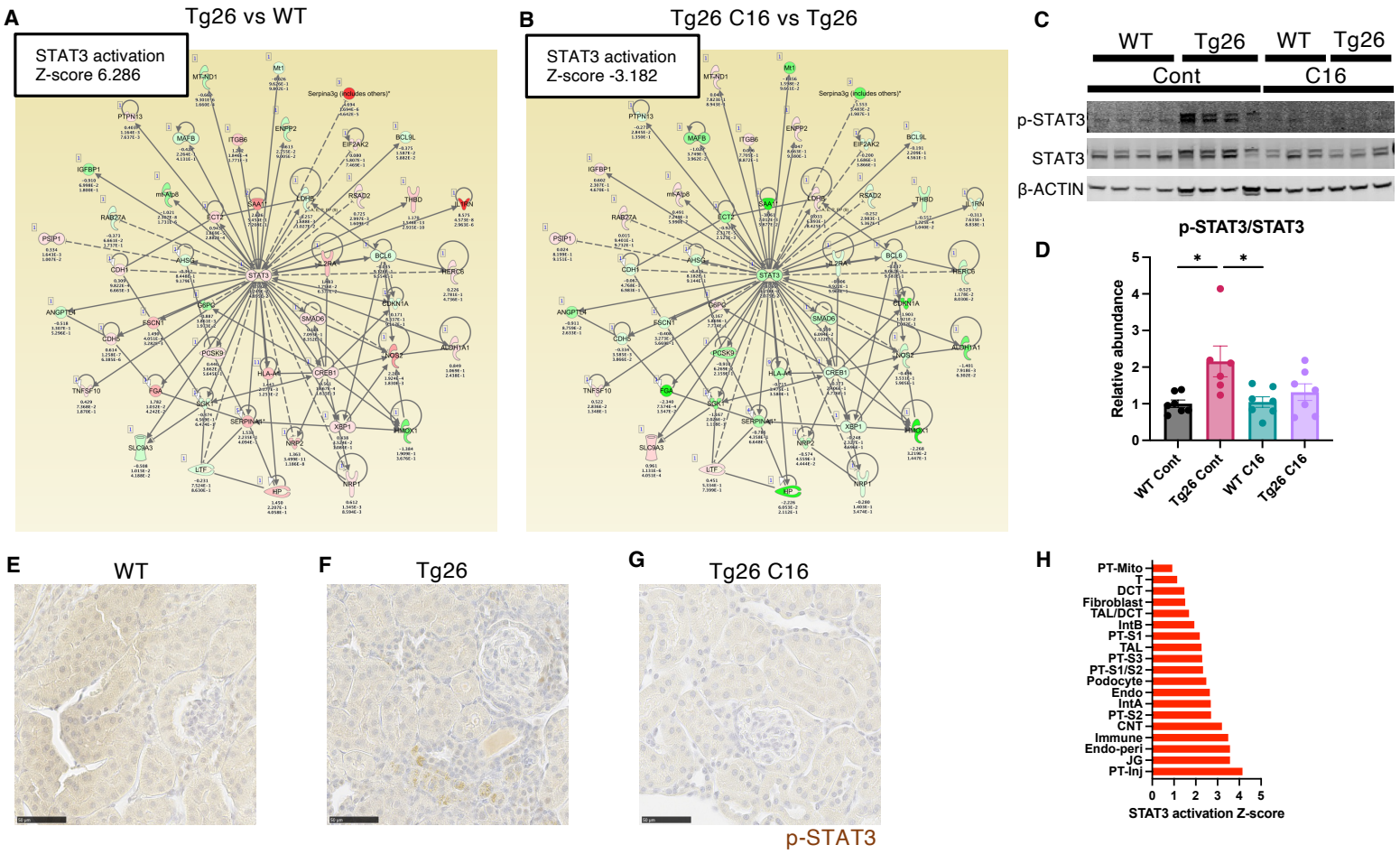


**Figure. 5 STAT3 activation downstream of PKR.**
(**A, B**) Mapping of STAT3 regulating genes comparing Tg26 vs WT (Z-score 6.286), Tg26 C16 vs Tg26 (Z-score -3.182) by bulk mRNA-seq. Red color indicates upregulation and green color indicates downregulation with log2-fold change, p-value, and adjusted p-value (FDR). Solid line indicates known positive regulation, dotted line indicates known negative regulation. (**C**) Representative immunoblotting of phospho-STAT3, STAT3 and β-ACTIN. (**D**) Quantitative results of phospho-STAT3/STAT3 by immunoblotting. (One-way ANOVA; *, P<0.05) (**E-G**) Immunohistochemistry of kidneys by phospho-STAT3 staining. (Scale bars are 50 μm) (**H**) STAT3 activation Z-score by IPA comparing Tg26 vs WT in each cluster by snRNA-seq.

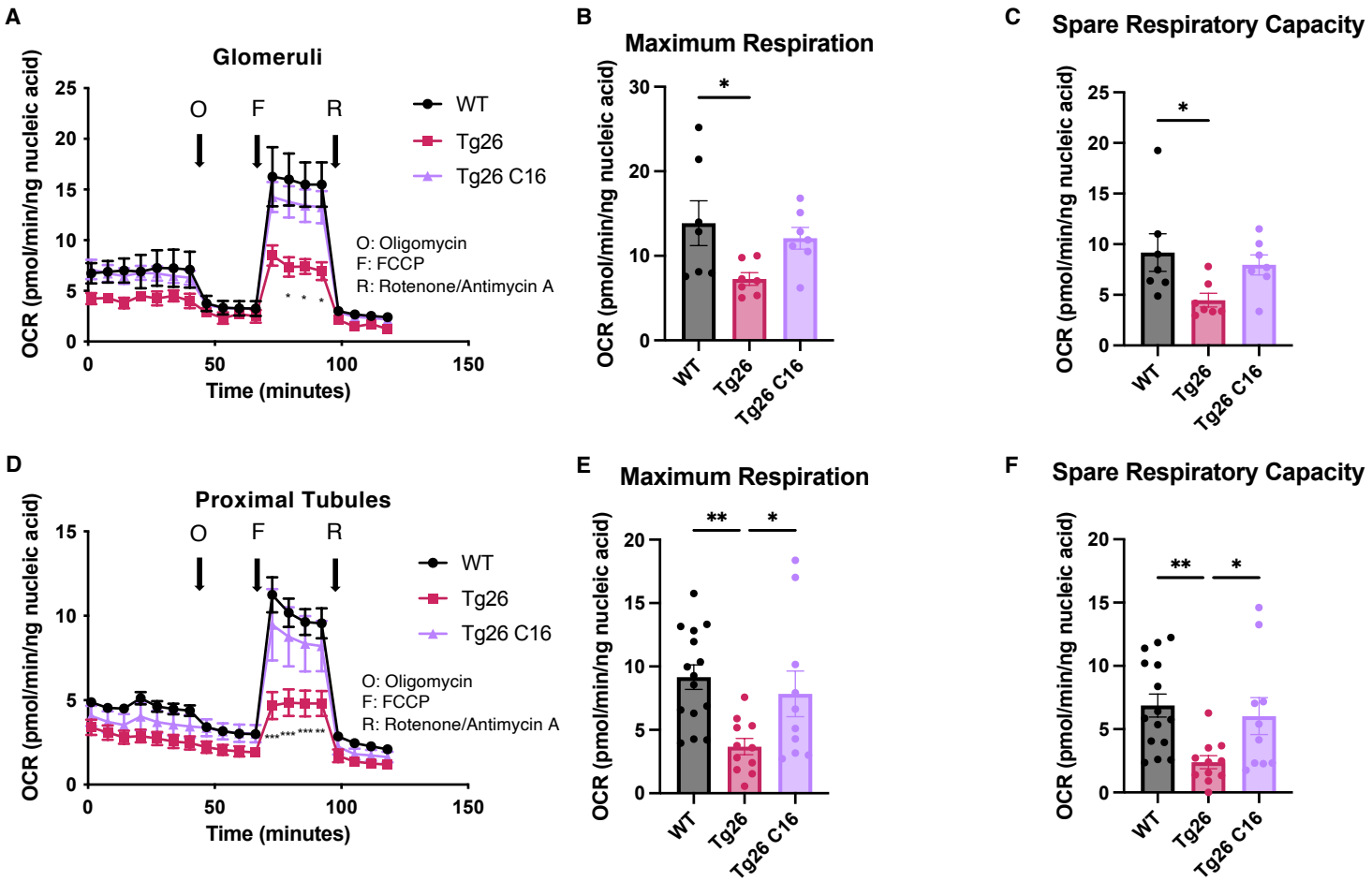


**Figure. 6 PKR inhibition with C16 reverses mitochondrial dysfunction in Tg26 glomeruli and proximal tubules.**
(**A**) Oxygen consumption rate (OCR) measurements with cell mito stress test using extracted glomeruli from WT, Tg26, C16 Tg26 kidney. (**B**) Maximum respiration rate calculated by OCR measurements of glomeruli. (**C**) Spare respiratory capacity calculated by OCR measurements of glomeruli. (**D**) Oxygen consumption rate (OCR) measurements with cell mito stress test using extracted proximal tubules from WT, Tg26, C16 Tg26 kidney. (**E**) Maximum respiration rate calculated by OCR measurements of proximal tubules. (**F**) Spare respiratory capacity calculated by OCR measurements of proximal tubules. (One-way ANOVA; *, P<0.05; **, P<0.01)

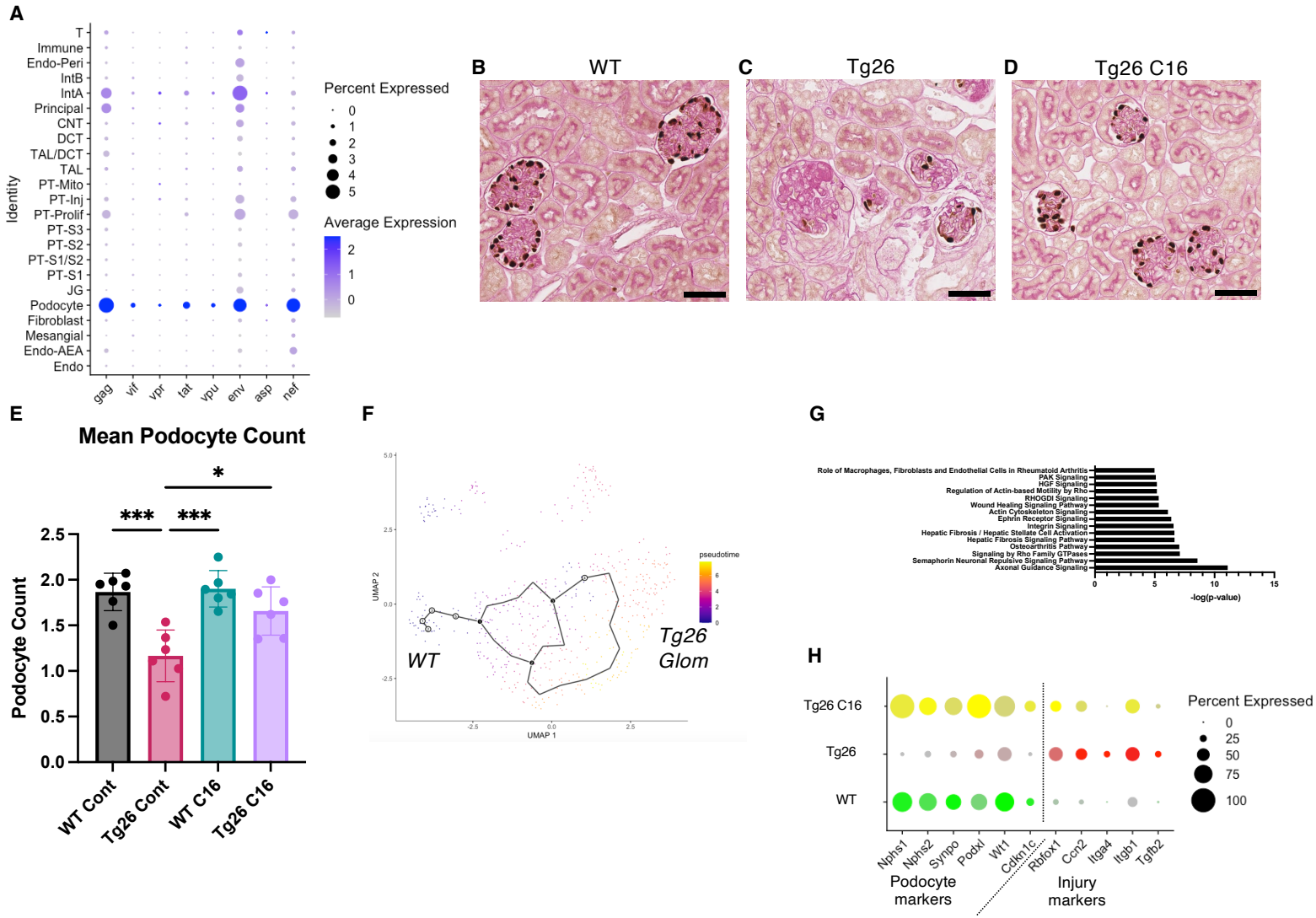


**Figure. 7 HIV-1 gene expression causes Tg26 podocytes dedifferentiation.**
(**A**) Dot plot showing HIV-1 gene expression levels in each cluster detected by snRNA-seq. (**B-D**) p57 staining of kidney showing podocyte loss and dedifferentiation. (Scale bars are 50 µm) (**E**) Podocount analysis showed podocyte loss in Tg26 and was rescued by C16. (One-way ANOVA; *, P<0.05; ***, P<0.001) (**F**) Trajectory analysis of podocytes by snRNA-seq data from WT, Tg26 glom samples. (**G**) Canonical pathway analysis results by IPA comparing Tg26 vs WT using snRNA-seq data from podocyte cluster. (**H**) Dot plot showing podocyte marker genes and representative differentially expressed genes in Tg26 podocytes by snRNA-seq.

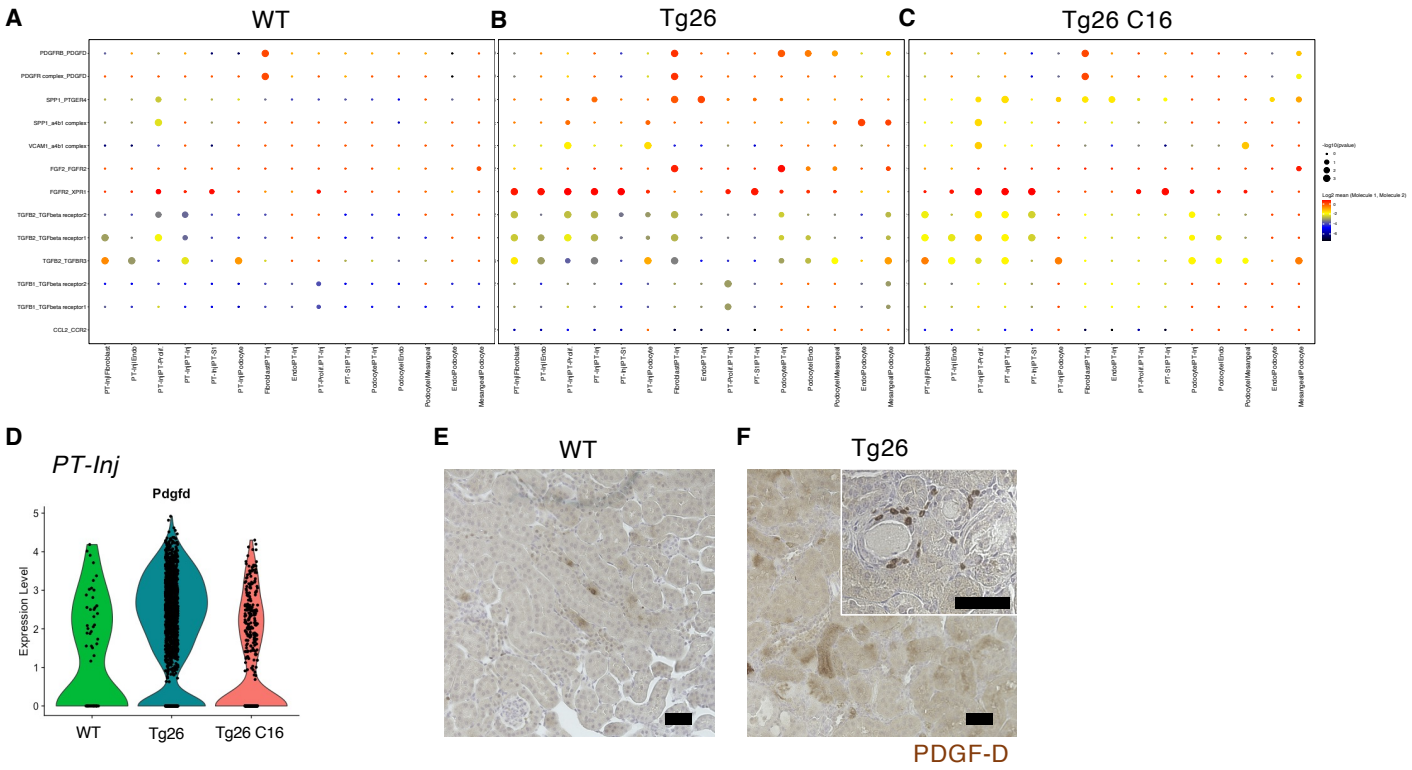


**Figure. 8 Cell-cell interaction analysis shows activated ligand-receptor interaction: PDGF-D-PDGFR-B pathway in Tg26.**
(**A-C**) Dot plots depicting results from cell-cell interaction analysis of WT, Tg26, C16 Tg26 snRNA-seq data.
(**D**) Violin plots showing Pdgfd expression levels in PT-Inj cluster. (**E**, **F**) Immunohistochemistry of kidneys by PDGF-D staining.
(Scale bars are 50 μm) .